FURTHER MICROSTRUCTURAL EXAMINATIONS OF V-4Cr-4Ti PRESSURIZED CREEP TUBES—

D. S. Gelles and R. J. Kurtz (Pacific Northwest National Laboratory)*

OBJECTIVE

The objective of this effort is to perform microstructural examinations of creep tubes to determine the deformation processes controlling thermal creep in vanadium alloys for comparison with creep response under irradiation.

SUMMARY

Pressurized thermal creep tubes of V-4Cr-4Ti have been examined following testing in the range 650 to 800°C for tests lasting ~10^4 h. Creep deformation was found to be controlled by climb-controlled dislocation glide at all temperatures below 800°C whereas at 800°C, sub-grain boundary structure predominated and represented the main obstacle for dislocation motion. At 650 and 700°C after ~10^4 h an increased density of (Ti,V) oxy-carbo-nitride precipitates near the outer surface extending inwards a distance of 30 and 70 μm, respectively, was found. At 800°C, enhanced (Ti,V) oxy-carbo-nitride precipitation was observed across the entire tube wall thickness and may have affected creep response. Also, evidence for internal precipitation associated with the dislocation structure could be identified. The discussion section addresses differences in the controlling creep mechanisms between grain boundary sliding, sub-grain boundary controlled dislocation climb and individual dislocation climb processes.

PROGRESS AND STATUS

Introduction

A series of pressurized V-4Cr-4Ti creep tubes have been tested under vacuum over the temperature range 650 to 800°C, [1-2] and selected failed specimens from those tests have previously been examined in order to identify operating creep and failure mechanisms [3-4]. It is now possible to examine specimens that have undergone testing up to ~10^4 hrs. This report provides microstructural examinations for tube specimens tested at 650°C to 200 and 250 MPa, at 700°C to 125 MPa, at 725°C to 150 MPa and at 800°C to 50 MPa.

Experimental Procedure

Specimens selected for examination are listed in Table 1. Detailed information on specimen preparation and testing procedures were reported previously [1,2]. Three of the tubes failed during testing, and therefore, the applied stress was removed while at temperature. The vacuum furnace was shut down immediately upon detecting a tube failure so the time at temperature in the unstressed condition was minimal. Two tubes did not fail and were allowed to cool while still under pressure.

Optical metallography was performed on all specimens using Murakami's etch (10 g. $K_3Fe(CN)_6$, 10 g NaOH, 100 ml H_2O for ~10sec). Specimen preparation for transmission electron microscopy (TEM) used standard punching, grinding and electropolishing procedures as described previously [4]. The punch was designed for tubular specimens with a radius of curvature of ~2.5 mm. Microscopy was performed on a Technai 30 TEM operating at 300 keV with the imaging procedures employed to provide Burgers vector anisotropy information [5]. Information on the direction of the principal stresses was retained during specimen preparation and examination.

---

*Pacific Northwest National Laboratory (PNNL) is operated for the U.S. Department of Energy by Battelle Memorial Institute under contract DE-AC06-76.

Table 1. Test conditions for specimens examined in this report

Specimen ID	Test temperature (°C)	Midwall effective stress (MPa)	Time to failure (h)	Effective mid-wall strain (%)	Comments on failure
AR02	650	200	10601	8.9	Burst
AR03	650	250	2733	4.4	Small hole
AR13	700	119	9663*	2.3	Did not fail
AR08	725	150	1506	5.0**	Burst
AR20	800	48	6052*	12.7	Did not fail

*Specimen did not fail. The time listed is the total time at temperature.

**Strain measured at 1221 h, since tube deformation associated with burst prevented an accurate strain measurement.

Table 2. Test conditions for specimens examined previously [4]

Specimen ID	Test temperature (°C)	Effective midwall stress (MPa)	Time to failure (h)	Effective mid-wall failure strain (%)
AR14	700	138.9	6667	14.8
AR15	700	158.8	2804	13.0
AR16	800	70.6	4029	51.9
AR17	800	92.6	864	13.6
AR18	800	117.7	578	24.1
AR19	800	136.8	242	14.7

Results

Metallography

Failure in specimens AR02 and AR08 resulted in large distortions so that the opening created by failure was about the size of the tube diameter (and described in Table 1 as a burst). Failure in specimen AR03 was more typical of that found previously in specimens AR14 and AR16 where only a small surface crack could be found [4]. Metallographic examinations revealed no major differences between creep conditions. Figure 1 provides optical metallographic examples of grain structure for different tubes tested at 650, 700 and 800°C. No change in grain size is evident for the different test temperatures.

Examination of the etched specimens demonstrated that the (Ti,V) oxy-carbo-nitride particles were observable and that an effect of the environment during testing could be seen. Examples of the microstructure near the outer surface of each specimen are shown in Fig. 2 with the outer diameter to the right in each case. From these images, a layer of enhanced precipitation extending ~30 μm into specimen AR02 was estimated. The enhanced precipitate layer extended ~70 μm into specimen AR13 and it probably extended all the way through specimen AR20. Therefore, creep tests at 650°C and 700°C were relatively unaffected by the testing environment, but tests at 800°C may have been affected by the environment.

Microscopy

All microstructures showed non-uniform grain structures, non-uniformly distributed coarse precipitation and low-to-moderate dislocation densities. Of concern was evidence in each specimen of dislocation rearrangement after specimen preparation such that near the perforation surface steps could be seen and long straight dislocations were present elsewhere in the microstructures. As a result, dislocation imaging was restricted to thicker areas where effects of dislocation rearrangement were much less evident. None-

the less, it is anticipated that all microstructures reported here have been affected by post-creep deformation.

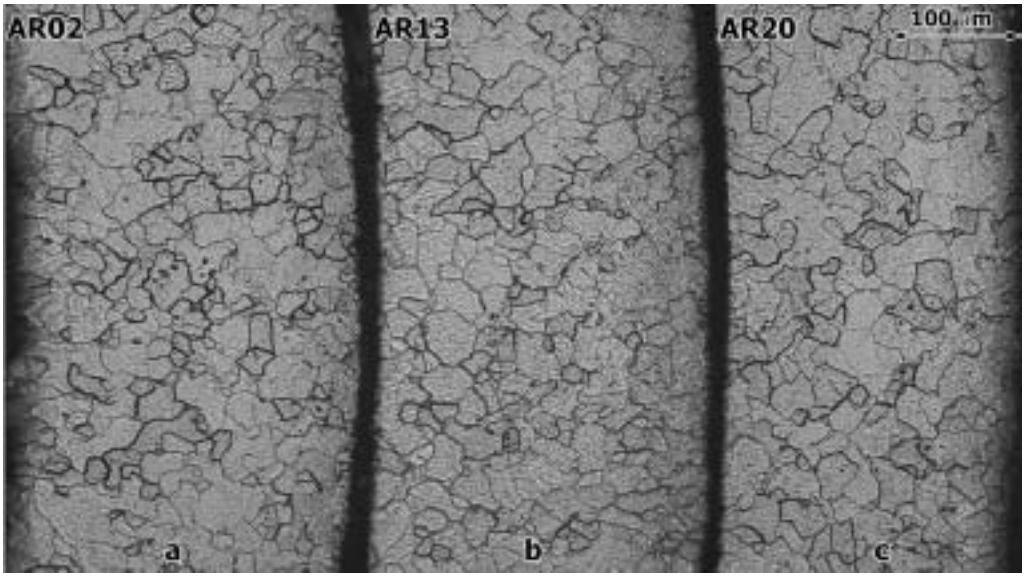

Fig. 1. Optical metallography of pressurized tube specimens a) AR02 tested at 650°C/200 MPa, b) AR13 tested at 700°C/119 MPa, and c) AR20 tested at 800°C/48 MPa.

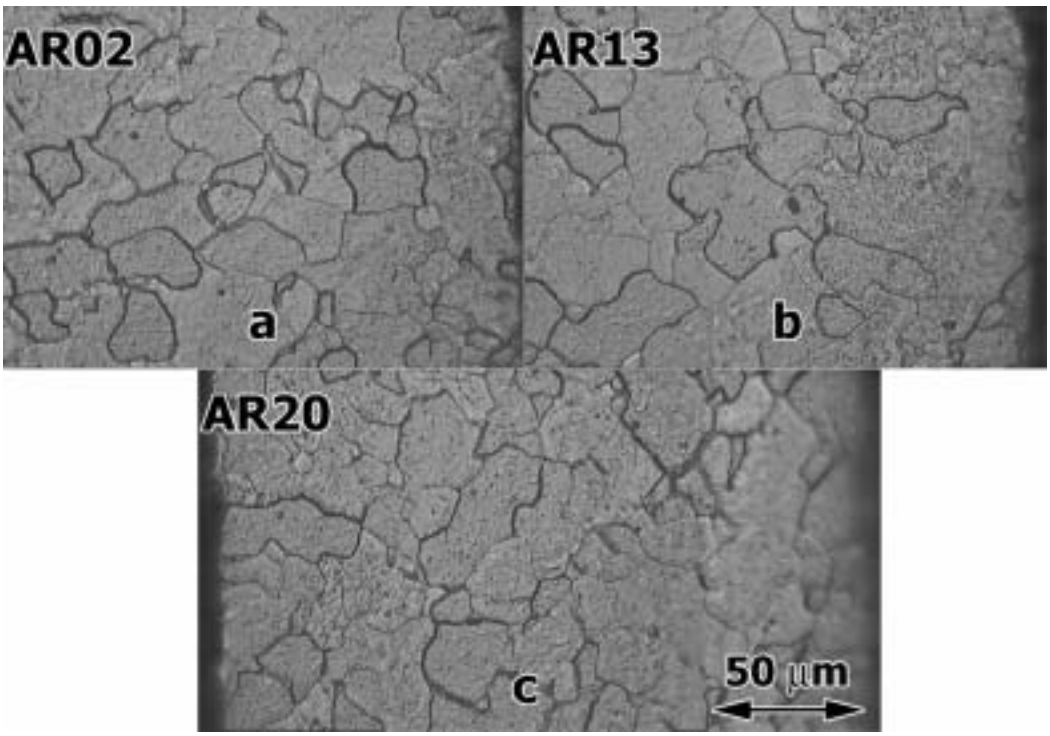

Fig. 2. Higher magnification optical metallography of pressurized tube specimens a) AR02 tested at 650°C/200 MPa, b) AR13 tested at 700°C/119 MPa, and c) AR20 tested at 800°C/48 MPa.

Lower magnification micrographs for the conditions examined are provided in Fig. 3 along with an example of the original tube structure to show dislocation and precipitate structures. Note that Fig. 3c of specimen AR03 is at a higher magnification than the rest. From Fig. 3, it can be demonstrated that moderately high dislocation densities are found for all conditions except AR20, 800°C/48 MPa, (Fig. 3f) where the dislocations tend to be confined to sub-grain boundaries. Precipitation of coarse (Ti,V) oxy-carbo-nitrides is non-uniform, but in the examples given in Fig. 3, the particle sizes are very similar and on the order of ~0.3 μm. It is apparent that these coarse precipitate particles were present prior to testing and did not change significantly during creep testing. However, Figs. 3c through 3f include examples of grain boundary structures where smaller precipitate particles can be seen and differences in particle size can be found. In fact, for condition AR20, the particles at grain boundaries have grown to about the same size as the rest of the particles. Such smaller particles on grain boundaries were present following the heat treatment of the tubing, [6] and therefore this size range is sensitive to coarsening on a time scale of ~10^4 hrs in the temperature range 650 to 800°C.

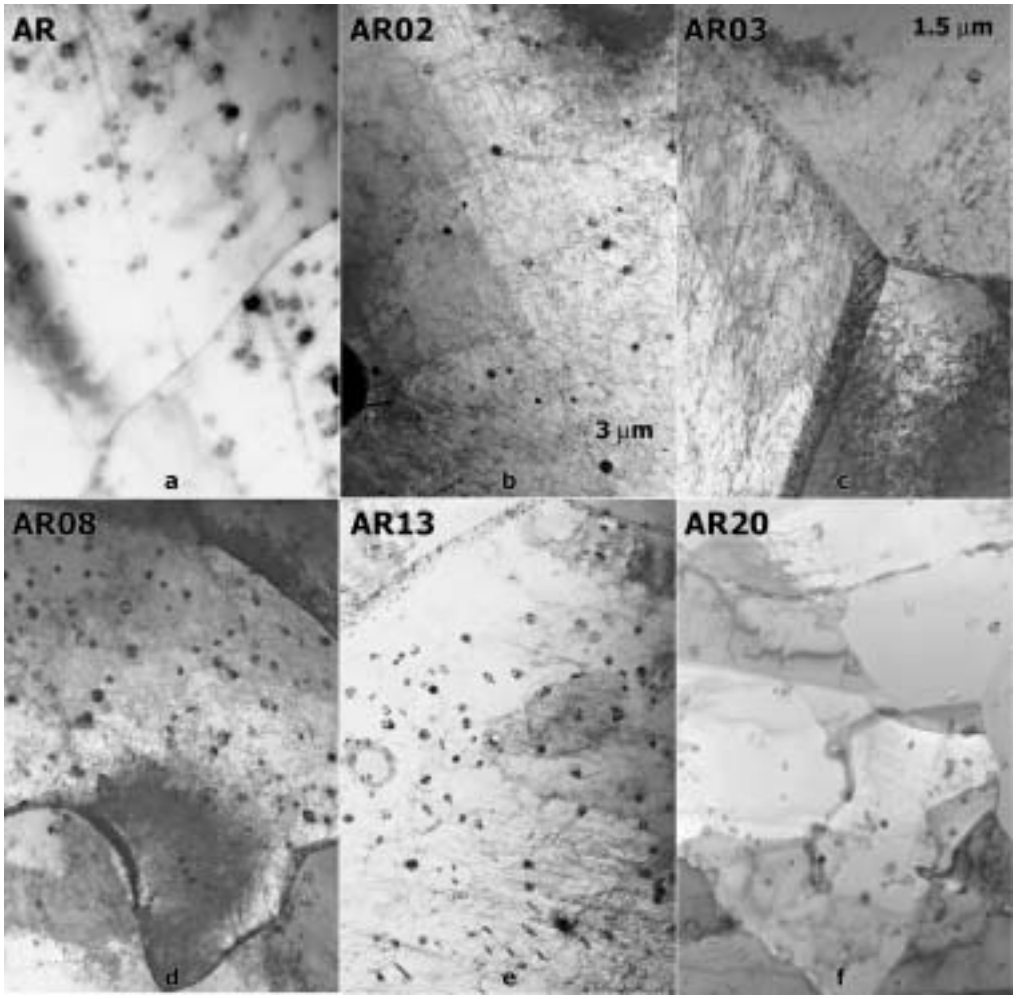

Fig. 3. TEM microstructures of pressurized tube specimens a) as heat treated, b) AR02 tested at 650°C/200 MPa, c) AR03 tested at 650°C/250 MPa, d) AR08 tested at 725°C/150 MPa, e) AR13 tested at 700°C/119 MPa, and f) AR20 tested at 800°C/48 MPa.

Examples of the dislocation structures found in each specimen are given in Figs. 4-8. In each case three views are provided with $\bar{g}=01\bar{1}$ and 200 always and either $\bar{1}10$ or $\bar{1}01$ depending on foil orientation. Also, as noted in reference [5], all $\frac{a}{2}$<111> Burgers vectors should be visible in 200 imaging, whereas only

half the possibilities are present in $01\bar{1}$, $\bar{1}10$ or $\bar{1}01$. By comparison of the three images that are provided, it should be possible to identify each of the four Burgers vectors present. Figure 4 gives an example of specimen AR02 tested at 650°C and 200 MPa, revealing a complex dislocation tangle. Two features denoting heterogeneous precipitation can be identified. Below the large precipitate at the upper left is an elongated feature that can only be seen in Figs. 4a and 4c and can be described as a linear precipitate array. Also, throughout the figure are small equiaxed dark features often associated with dislocations. It is anticipated that these are small precipitates that affect creep response.

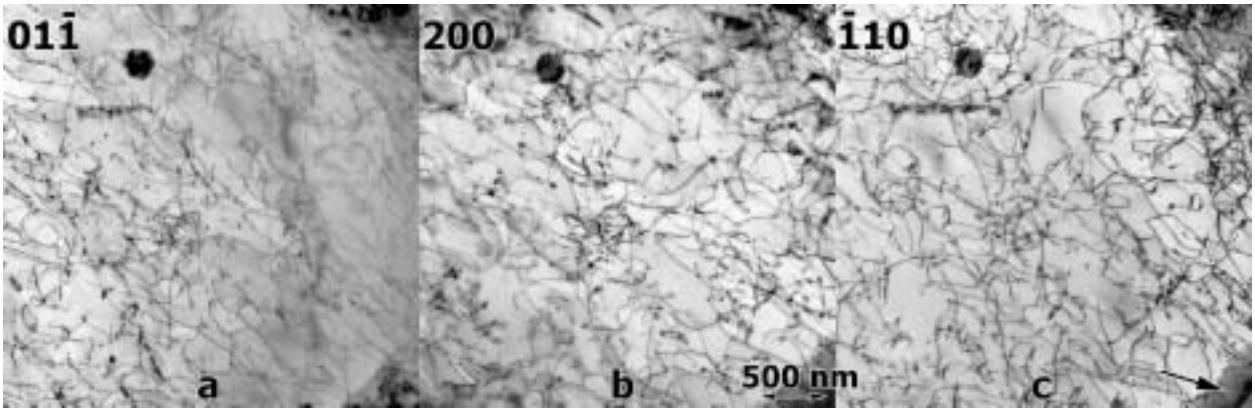

Fig. 4. Dislocation imaging for specimen AR02 (650°C/200 MPa) with $\bar{g}=\bar{1}10$ horizontal in a), $\bar{g}=200$ vertical in b), and $\bar{g}=\bar{1}10$ as indicated in c).

Figure 5 shows similar features in specimen AR03, tested at the same temperature as for AR02, but at higher stress and for a shorter time. In this case more of the planar precipitate arrays can be identified, and the dislocation density is non-uniform, enhanced near larger 0.3 μm precipitate particles.

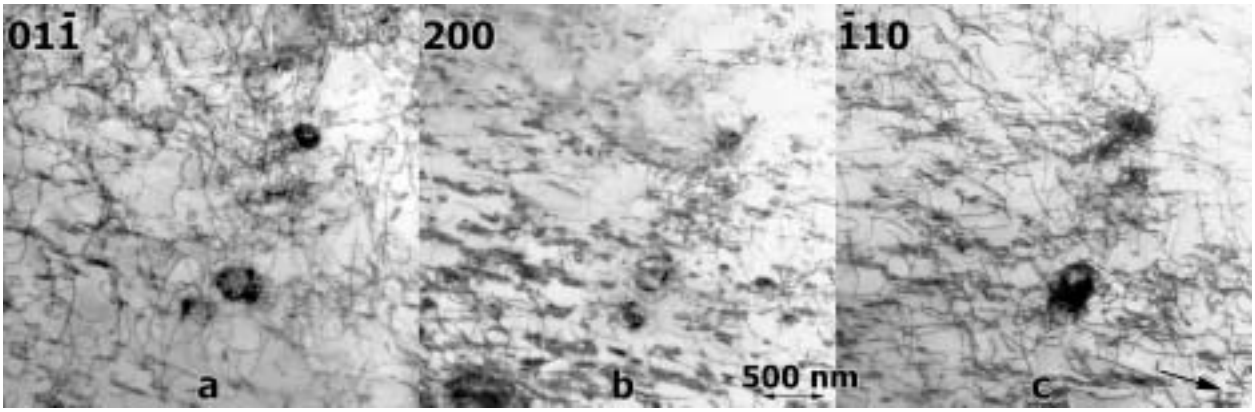

Fig. 5. Dislocation imaging for specimen AR03 (650°C/250 MPa) with $\bar{g}=\bar{1}10$ horizontal in a), $\bar{g}=200$ vertical in b), and $\bar{g}=\bar{1}10$ as indicated in c).

Figure 6 provides similar views of specimen AR13 tested at 700°C. Again, equiaxed fine precipitation can be identified, and the dislocation density is non-uniform. In fact, the dislocation array in the center of each micrograph consists of a network, with only some of the line segments showing in 6a and 6c.

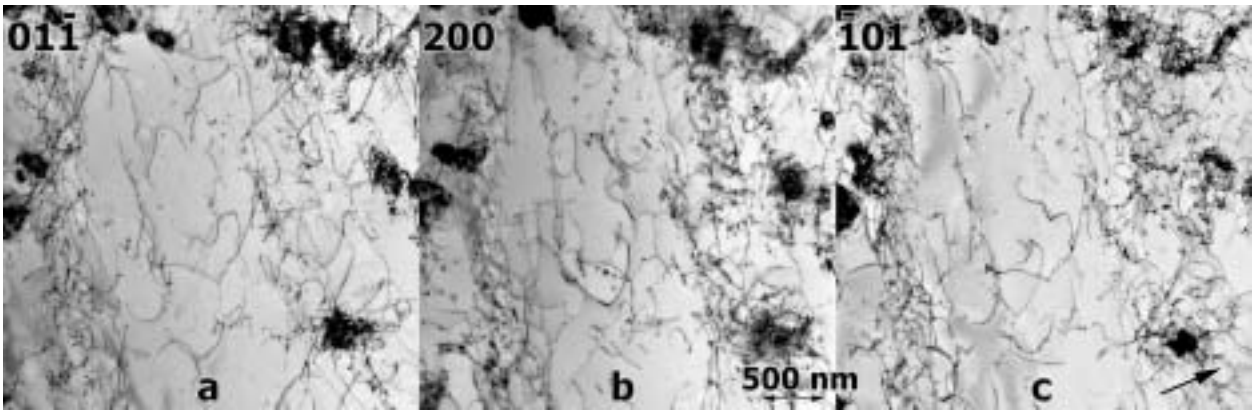

Fig. 6. Dislocation imaging for specimen AR13 (700°C/119 MPa) with $\bar{g}=\bar{1}10$ horizontal in a), $\bar{g}$=200 vertical in b), and $\bar{g}=\bar{1}01$ as indicated in c).

Figure 7 shows specimen AR08 tested at 725°C. Again, fine precipitation is present and examples of coarser precipitation in planar arrays can be identified. A higher density of straight dislocations can be seen in this view, which may be an example of post-creep testing deformation. Note that these straight dislocations running from upper right to lower left are only observable in Figs. 7a and 7b, indicating that they have Burgers vector $\frac{a}{2}[1\bar{1}1]$ as can be demonstrated from information in reference [6], and as can be shown are primarily edge in character. As post-creep deformation is expected to leave dislocations of screw character, these longer straight dislocations were probably generated by climb during the creep process.

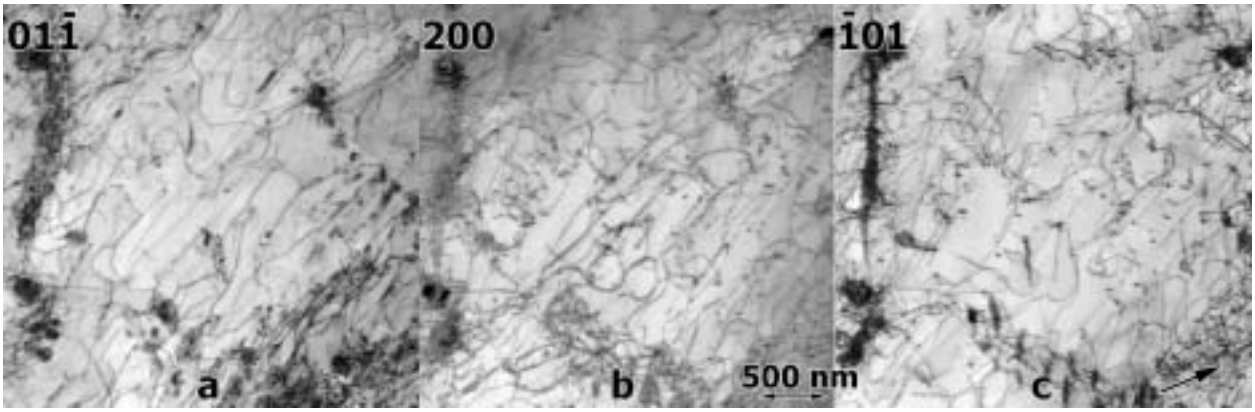

Fig. 7. Dislocation imaging for specimen AR08 (725°C/150 MPa) with $\bar{g}=\bar{1}10$ horizontal in a), g=200vertical in b), and $g=\bar{1}01$ as indicated in c).

Figure 8 shows sub-grain boundary structure in specimen AR20, tested at 800°C. The area is unusual because a small sub-grain about 2 μm in diameter is seen. Most sub-grains are much larger. The upper boundary for this sub-grain is probably a simple array of dislocations of only one Burgers vector and examples can be identified where dislocations in this array are interacting with other dislocations and are being pulled into or out of the sub-grain. Also, an array of dislocations can be seen towards the lower part of the sub-grain that could be an example of post-creep deformation, but in fact, these dislocations form a network, visible in Figs. 8a and c and therefore, the sub-grain is sub-divided. (The fact that this complete network cannot be see in Fig. 8b either means that the imaging in this area is not really controlled by $\bar{g}$=200 or that a different Burgers vector such as a[200] is present.) Finally, the dislocation arrays typical of sub-grain boundary structure defining the lower right side of the sub-grain (and the one

defining the lower left) are complex arrays with several Burgers vectors present at a high dislocation density. This is indicated by the cross-hatched nature to the boundary imaging. Such boundaries have incorporated many dislocations with at least two Burgers vectors represented as the dislocation structure has relaxed into this lower energy state.

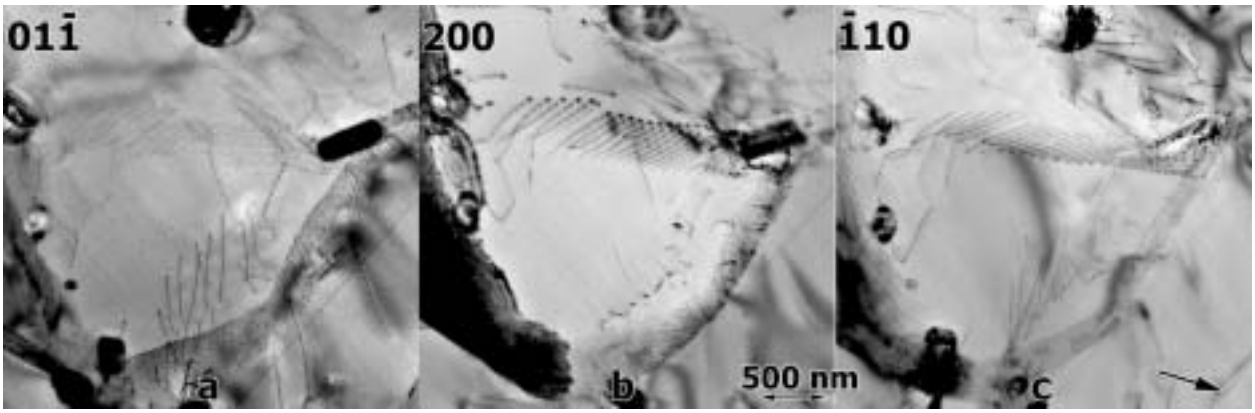

Fig. 8. Dislocation imaging for specimen AR20 (800°C/48 MPa) with $\bar{g}=\bar{1}10$ horizontal in a), $\bar{g}=200$ vertical in b), and $\bar{g}=\bar{1}10$ as indicated in c).

It can be noted that an interesting sub-grain boundary was identified in specimen AR13 tested at 700°C and shown in Fig. 9. The array of dislocations forming the sub-grain boundary happens to be close to a grain boundary on the lower left, but the orientation is almost orthogonal. The dislocation array in the boundary is simple, with one burgers vector predominating. (As the sub-boundary can be seen in both 200 and $\bar{1}01$ views, the Burgers vector should be $\frac{a}{2}[\bar{1}11]$ and of predominantly edge character, similar to the example described for Fig. 7.)

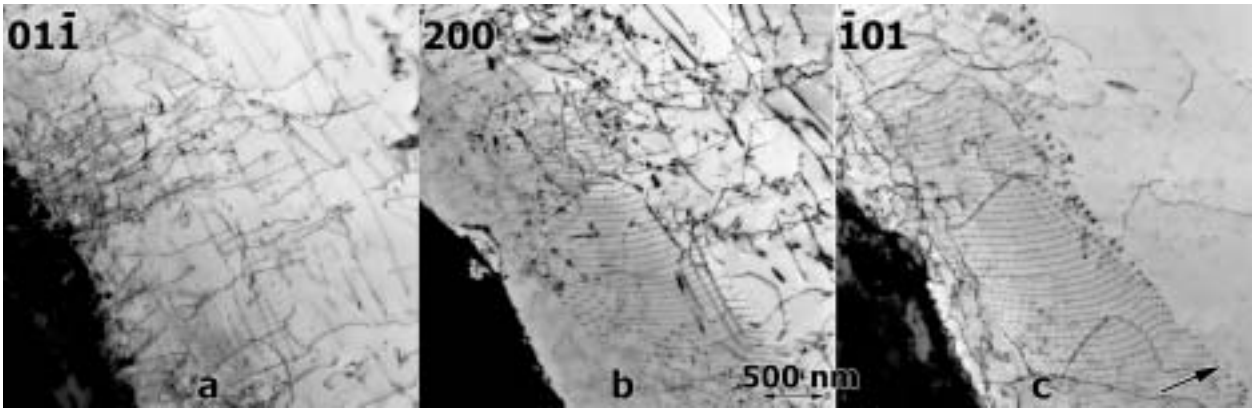

Fig. 9. Dislocation imaging for specimen AR13 showing a sub-grain boundary with $\bar{g}=\bar{1}10$ horizontal in a), $\bar{g}=200$ vertical in b), and $\bar{g}=\bar{1}01$ as indicated in c).

Discussion

The metallographic results shown in Fig. 2 indicate that impurity pickup from the vacuum has produced enhanced precipitation near the surface for tests at 650 and 700°C to ~10^4 hr. An estimate of the amount of impurity pickup can be obtained from the oxygen and nitrogen partial pressures in the vacuum furnace. Each test specimen was wrapped in Ti foil and the total vacuum pressure was ≤10^{-7} torr during high-temperature testing. Residual gas analysis at 800°C indicates that the oxygen and nitrogen partial pressures were about 2×10^{-10} torr (2.7×10^{-8} Pa). Pint and DiStefano [7] have developed an oxidation

model for V-4Cr-4Ti that gives the rate of oxygen pickup in mg/cm^{2}h at a given oxygen partial pressure and temperature. Their model is pertinent to the test conditions employed here. The equation fit to their data is:

$$r = 4.7x10^2 e^{-821/T} p(O_2) \quad (1)$$

where $p(O_2)$ is the oxygen partial pressure in Pa and T is the temperature in Kelvin. The surface area of a creep tube is about 3.65 cm^2 so at a temperature of 650°C the amount of oxygen picked up in ~10^4 h is 0.19 mg. At 800°C the amount of oxygen picked up is 0.22 mg. In terms of wppm the estimated oxygen pickup ranges from 360 to 415 wppm. Similar estimates of oxygen pickup can be obtained from the flux of oxygen atoms impinging on the surface of the specimen during the course of the experiment. From the kinetic theory of gases the flux of oxygen atoms, J, is:

$$J = \frac{P}{(2\pi mkT)^{1/2}} \quad (2)$$

where P is the oxygen partial pressure, m is the mass of an oxygen atom, k is Boltzmann's constant and T is the absolute temperature. At 800°C the amount of oxygen picked up after ~10^4 h of exposure predicted by Equation 2 is 0.20 mg. The estimated levels of oxygen gain during our creep experiments compare favorably with actual experimental measurements. Kurtz and Hamilton [1] measured the oxygen pickup after 5142 h at 800°C at 345 wppm. The measured pickup of nitrogen was much less, only 15 wppm.

At 650 and 700°C the thickness of enhanced precipitation layers are about ~13 and 30% of the creep tube wall thickness, respectively. Therefore, for specimen AR13 tested at 700°C, about 70% of the specimen was deforming towards the end of the test in a manner typical of the starting interstitial content. However, it is interesting to note that for specimen AR20, although interstitial pick-up occurred all the way through the tube, the net consequence was only a modest increase in precipitate particle number density, because coarsening in this specimen produced precipitates comparable in size with the original distribution, at only a modest increase in number density. [The distribution of particles appears similar throughout Fig. 2c in comparison with the distribution away from the surface affected regions in Figs. 2a and b.] It should be noted that interstitial pickup did not play a significant role in our determination of secondary creep rates (see below) since calculation of the secondary creep rate were based on data gathered very early in the test when interstitial impurity pickup was negligible.

To put these observations into perspective, we have calculated the effective diffusion of oxygen and nitrogen through the wall of a pressurized tube. Two estimates were found for diffusion of oxygen in relevant vanadium alloys, V-5Ti [8] and V-5Cr-5Ti [9]. Data on nitrogen diffusion in V-5Cr-5Ti were not available so its diffusivity was estimated from information on oxygen and nitrogen diffusion in pure vanadium. The diffusivity of nitrogen in pure vanadium is about 15 times lower than oxygen at 650°C and about 10 times lower at 800°C [10]. Assuming the diffusion of nitrogen in V-5Cr-5Ti is lower than oxygen by an amount equal to the ratio of the nitrogen-to-oxygen diffusivity in pure vanadium an estimate of the effective diffusion distance for nitrogen in the alloy can be obtained. The results are summarized in Table 3. From these results, it is apparent that oxygen can diffuse through a pressurized tube with a wall thickness of 0.254 mm several times during the course of a creep test, even at 650°C. The diffusion distance of nitrogen is estimated to be much smaller than oxygen and may account for the observed precipitate distributions. Chemical analysis of the near surface precipitates will be performed to see if this hypothesis can be confirmed.

Table 3. Calculations for the effective diffusion distance of oxygen and nitrogen under conditions relevant to pressurized V-4Cr-4Ti creep tubes

Alloy	D_o (m^2/sec)	Q (kJ/mol)	Temp (°C)	D (m^2/sec)	x=√Dt (mm)
Oxygen					
V-5Ti [8]	$3.1x10^{-4}$	172	650	$5.88\ x10^{-14}$	1.5
V-5Cr-5Ti [9]	$1.3x10^{-7}$	120	650	$2.05\ x10^{-14}$	0.9
V-5Ti [8]	$3.1x10^{-4}$	172	800	$1.34x10^{-12}$	5.4
V-5Cr-5Ti [9]	$1.3x10^{-7}$	120	800	$1.83x10^{-13}$	2.0
Nitrogen					
V-5Cr-5Ti			650	$1.37x10^{-15}$	0.2
V-5Cr-5Ti			800	$1.83x10^{-14}$	0.6

In our previous work [3,4], two types of deformation microstructures were found. The first type exhibits the characteristics of the microstructures presented here in Figs. 4-7 and the second type is similar to the microstructure shown in Fig. 8. Figure 10 provides a plot of the stress dependence for creep with the data points corresponding to microstructural examinations labeled. The microstructures of specimens AR16 and AR20 show well-developed sub-grains, whereas all other specimens exhibit dislocation tangles and poorly defined sub-grains. From Fig. 10, it is clear that specimen AR20 is creeping with a lower stress dependence of ~0.8 in comparison with the other conditions examined where the stress dependence is ~4. Specimen AR16 appears to be in a transition region and this may explain why the dislocation density within sub-grains in this specimen was moderate, in contrast to observations in specimen AR20 shown in Fig. 3e where dislocation structures were almost entirely in sub-grain boundaries. The microstructural differences clearly correspond to changes in creep mechanism. Previously, [1,2] we attributed the creep response in the high-stress exponent regime to some form of dislocation climb controlled process and in the low-stress exponent region to processes involving grain boundary sliding, Coble creep, or some combination of the two. The culmination of our microstructural observations indicates that creep in the high-stress exponent region is due to a viscous glide rather than a climb controlled mechanism. Such a conclusion is consistent with many of our observations. As noted by Mohamed and Langdon, [11], creep of solid solution alloys controlled by a dislocation climb mechanism should be similar to that of pure metals, namely, 1) the stress exponent is close to 5, 2) an instantaneous strain occurs on application of the load, 3) the creep curve exhibits normal primary creep, 4) the steady-state creep rate is dependent on the stacking fault energy of the alloy, and 5) a regular array of sub-grains is formed during creep. When creep of solid solution alloys is controlled by a viscous glide process features different from those observed in pure metals are found, namely, 1) the stress exponent is close to 3, 2) there is little or no instantaneous strain on application of the load, 3) the creep curve enters the steady-state region almost immediately, 4) the steady-state creep rate appears to be independent of the stacking fault energy of the alloy, and 5) sub-grains are not generally formed during creep or, if formed, are less extensive than in pure metals. Mohamed and Langdon, [11], developed a simple criterion to determine under what conditions a solid solution alloy would favor glide-controlled creep over climb-controlled creep. The criterion for viscous glide controlled creep is:

$$\frac{B\sigma^2}{k^2(1-\nu)}\left(\frac{\gamma}{Gb}\right)^3 > \frac{T^2}{e^2cb^6} \tag{3}$$

where $B \sim 8x10^{12}$, σ is the stress, k is Boltzmann's constant, ν is Poisson's ratio, γ is the stacking fault energy, G is the shear modulus, b is the Burgers vector, T is the temperature, e is the solute-solvent size difference and c is the solute concentration. Assuming that Ti is the solute controlling viscous glide, taking the stacking fault energy for V-4Cr-4Ti to be 0.2 J/m^2 [12], using a stress of 100 MPa at a temperature of 1000 K one obtains a prediction that creep of V-4Cr-4Ti in the high stress regime should

be predominantly viscous glide controlled since the left hand side of Eq. 3 gives a value of ~$5x10^{57}$ compared to the right hand side, which is ~10^{55}.

Finally, it should be noted that at low stresses, if the stress exponent for creep approaches 1, as shown in Fig. 10, then a change in creep mechanism to grain boundary sliding or Coble creep is expected [13,14]. If creep is controlled by the stress-directed flow of vacancies, with diffusion along grain boundaries (Coble), then Langdon [14] notes that such creep can be identified by examining the microstructure for grain elongations, with denuded zones at boundaries in tension and associated precipitate pile-ups at boundaries in compression. Specimen AR20 provides a test, given 12.7% diametral strain. If diffusion creep is significant, then the metallographic images in Figs. 1c and 2c should reveal grain elongation in tangential directions and precipitate pile-ups on grain boundaries parallel to the tangential direction. Careful examinations reveal no precipitate pile-ups suggesting that creep in the low-stress regime is controlled by grain boundary sliding processes possibly accommodated by lattice or grain boundary diffusion. A further test of this hypothesis would be to determine grain aspect ratios before and after creep testing. No change in grain aspect ratios should occur if grain boundary sliding is the predominant creep mechanism at low stresses. Furthermore, observation of well-defined subgrains is indicative of significant dislocation motion and rearrangement during creep, not expected for grain boundary sliding or Coble creep. In future work, we intend to consider the possibility of Harper-Dorn creep [15] controlling this behavior despite the lower temperature regime.

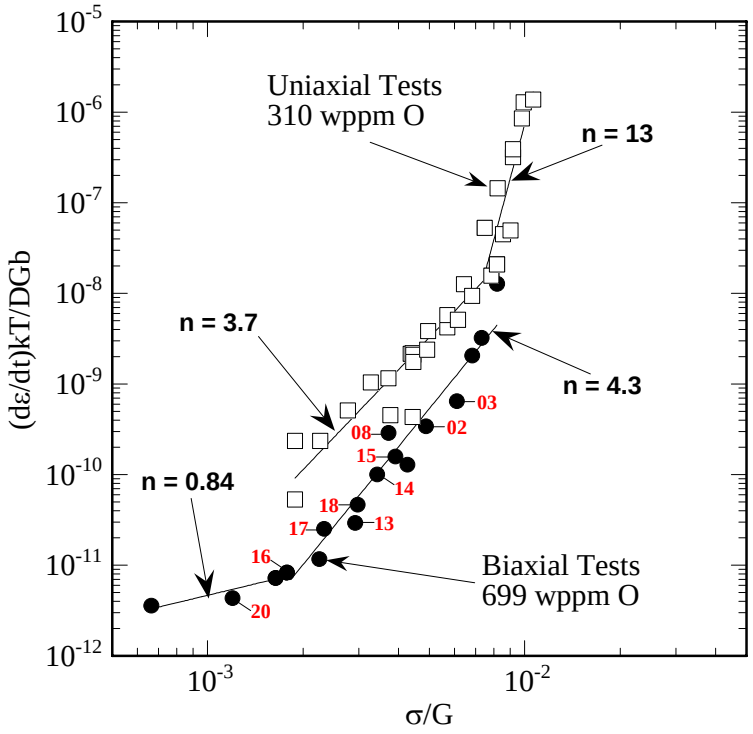

Fig. 10. Stress dependence of the normalized effective mid-wall creep strain for unirradiated vanadium alloys, with pressurized tube specimens chosen for microstructural examination identified by number.

Results

Five pressurized tubes of V-4Cr-4Ti have been examined following thermal creep testing to ~10^4 hr in the temperature range 650-800°C in order to understand the mechanisms controlling creep. It is found in all

cases that creep is controlled by dislocation motion. But the mechanism changes with increasing temperature from one controlled by the climb and interaction of individual dislocations, to one controlled by sub-grain boundary structure that is created by relaxation of the interacting dislocations to a lower energy planar array.

Evidence for an increased density of (Ti,V) oxy-carbo-nitride precipitates near the outer surface extending inwards a distance of 30 and 70 μm, respectively, was found after 650 and 700°C after ~10^4 h. At 800°C, enhanced (Ti,V) oxy-carbo-nitride precipitation was observed across the entire tube wall thickness and may have affected creep response. Calculations provide prediction that nitrogen contamination may be responsible. Also, evidence for internal precipitation associated with the dislocation structure could be identified.

The mechanism controlling creep behavior at higher stresses/lower temperatures is shown to most likely be viscous glide controlled creep arising from the presence of Ti and Cr solid solution hardening. The mechanism controlling behavior at lower stresses/higher temperatures should be grain boundary sliding or Coble creep, but given evidence for extensive dislocation production and rearrangement, consideration is being given to the alternate explanation of Harper-Dorn creep.

Future Work

The effort will be continued as opportunities become available.

References

[1] R. J. Kurtz and M. L. Hamilton, DOE/ER-0313/25 (1999) 7.
[2] R. J. Kurtz, A. M. Ermi, and H. Matsui, DOE/ER-0313/31 (2002) 7.
[3] D. S. Gelles, M. L. Hamilton, and R. J. Kurtz, DOE/ER-0313/26 (1999) 11.
[4] D. S. Gelles, DOE/ER-0313/31 (2001) 12.
[5] D. S. Gelles, A. Kimura, and R. J. Puigh, DOE/ER-0313/12 (1992) 123.
[6] D. S. Gelles and H. Li, DOE/ER-0313/19 (1996) 22.
[7] B. A. Pint and J. R. DiStefano, J. Nucl. Mater. 307-311 (2002) 560.
[8] H. Nakajima, S. Nagata, H. Matsui, and S. Yamaguchi, Phil. Mag. A67 (1993) 557.
[9] M. Uz, K. Natesan, and V. B. Hang, J. Nucl. Mater. 245 (1997) 191.
[10] F. A. Scmidt and J. C. Warner, J. Less-Common Metals 26 (1972) 325.
[11] F. A. Mohamed and T. G. Langdon, Acta Mater. 22 (1974) 779.
[12] M. S. Duesbury and V. Vitek, Acta Mater. 46 (1998) 1481.
[13] R. L. Coble, J. Appl. Phys. 34 (1963) 1679.
[14] T. G. Langdon, in Creep Deformation: Fundamentals and Applications, Eds., R. S. Mishra, J. C. Earthman, and S. V. Raj, TMS, Warrendale Pa. (2002) 41.
[15] J. Harper and J. E. Dorn, Acta Met. 5 (1957) 654.